Structural color from a coupled nanowire pair beyond the bonding and antibonding model

Li, Q.; Wu, T.; van de Groep, J.; Lalanne, P.; Brongersma, M.L.

optica

Structural color from a coupled nanowire pair beyond the bonding and antibonding model

QITONG LI,[1] TONG WU,[2] JORIK VAN DE GROEP,[1] PHILIPPE LALANNE,[2] [iD] AND MARK L. BRONGERSMA[1,*]

[1]Geballe Laboratory for Advanced Materials, Stanford University, Stanford, California 94305, USA
[2]LP2N, CNRS, University of Bordeaux, 33400 Talence, France
*Corresponding author: brongersma@stanford.edu

Optical resonances in nanostructures can be harnessed to produce a wide range of structural colors. Conversely, the analysis of structural colors has been used to clarify the nature of optical resonances. Here, we show that silicon nanowire (NW) pairs can display a wide range of structural colors by controlling their radiative coupling. This is accomplished by exciting a series of Fabry–Pérot-like modes where light is repeatedly scattered between two NWs. These modes are beyond the expectation from the conventional chemical bonding model under a quasi-electrostatic approximation, in which only bonding and antibonding modes can be formed in a pair system through modal hybridization. The additional eigenmodes found in a two-resonator system originate from the nonlinear, frequency-dependent coupling strength derived from the radiative nature of low-Q resonators. The Fabry–Pérot modes can be tuned across the entire visible frequency range by varying the distance between two NWs, leading to what we believe is a new type of universal building blocks that can provide structural color within a subwavelength footprint. The presented results pave the way toward the design and usage of highly tunable resonances that exploit the radiative coupling of high-index nanostructures.   © 2021 Optical Society of America under the terms of the OSA Open Access Publishing Agreement

1. INTRODUCTION

The discovery of new mechanisms to create color have always been at the heart of human society—from colorful cave paintings in prehistoric times to advanced metasurface displays with a wide color gamut in modern life [1]. Nowadays, it is well understood that the intrinsic color of most materials originates from optical absorption in parts of the visible light spectrum due to electronic transitions in the associated media (pigments) [2]. Inspired by such resonant optical transitions in materials, additional geometry-induced optical resonances have been explored to carefully manipulate the angular, spectral, and polarization-dependent property of the scattered light, and create structural color [3]. Compared to pigments, these structural colors are chemically more stable, and have highly designable spectra as well as the potential for dynamic tuning [4]. Photonic crystals [5–7] are well known to produce structural colors [8–11], as the periodic distribution of the dielectric constant in photonic crystals gives rise to a photonic band structure that only reflects/transmits light in well-defined angular and frequency ranges [5–7]. However, a relatively large footprint is required to realize efficient color filtering due to the coherent interaction of many unit cells. More recently, individual nanoparticles have also been shown to produce structural color, and offer improved control over color spatially due to their nm-scale footprint [12–24]. This is attributed to the fact that metallic [12–19] or dielectric [20–24] nanoparticles and nanowires (NWs) support plasmon

or Mie resonances that can strongly scatter light at their resonant frequencies. The resonant frequency of such nanostructures is controlled through the choice of their size, shape, and material. Precise control over the scattering spectrum thus requires state-of-the-art nanofabrication techniques like electron-beam lithography or nanoimprint lithography [25,26].

Unlike the well-studied light scattering properties of periodic photonic crystals and individual nanoparticles mentioned above, we focus on the emergent optical properties of pairs or small clusters. In these systems, color generation results from the nontrivial electromagnetic interactions of nanoresonators. These systems combine the benefits of a subwavelength footprint with the broad tunability of periodic structures. Conventionally, an equivalent chemical bonding model [27–30] is used to describe the optical coupling between nanoresonators and the associated structural colors [13,31–33]. Under a quasi-electrostatic approximation, only bonding and antibonding modes can be formed in a pair system through modal hybridization. Significant shifts of the resonance frequency (or splitting thereof) is only expected when the optical near fields strongly overlap (i.e., two nanoresonators are extremely close to each other) [34–37]. However, a series of studies in scattering properties of metallic nanoparticle pairs/arrays [38–41] suggest that, besides the radiative decay of plasmon resonances, the spectral shape of the scattered light can also be modulated, even in the absence of near-field coupling. Although the spectral shifts are found to be small for zero-dimensional (0D) nanoparticle pairs

due to the inefficient radiative coupling, these results indicate the possibility of realizing structural color if a strong radiative coupling can be achieved between two nanoresonators. Radiative coupling has also proven to be important in coupled silicon (Si) NW systems and facilitated the creation of angle-sensitive detection systems [42].

Here, we demonstrate both theoretically and experimentally that Si NW pairs can display structural colors across the entire visible spectral range by controlling their radiative coupling. A series of additional Fabry–Pérot-type modes [43] can be formed as a consequence of iterative light scattering between two neighboring NWs [44]. These quasinormal modes (QNMs) [45] cannot be predicted by the conventional chemical hybridization model, which exhibits/predicts only bonding and antibonding modes. Instead, a nonlinear frequency-dependent Green's function must be used to describe the coupling between two neighboring NWs. The resonant frequency of the fundamental Fabry–Pérot mode is strongly shifted with respect to the original resonant frequency of a single NW, even in the absence of evanescent-field coupling. The resonant frequency can be tuned controllably across the entire visible frequency range by changing the distance between the two NWs while preserving significant color purity. Therefore, a NW pair with fixed NW dimensions can function as a universal building block for structural color, while maintaining a subwavelength footprint. We further envision that a tunable structural color can be realized through the use of stretchable substrates or microelectromechanical devices (MEMS) [46,47], therefore leading to a potential nanoscale dynamic color control platform.

2. RESULTS

We start our analysis by considering an individual square cross-sectional Si NW, which supports a range of leaky Mie-type optical resonances [48,49]. By performing a QNM analysis of the scattering spectrum of the NW, we find that its optical response is dominated by the fundamental TM_{11} QNM. As shown in the inset of Fig. 1(b), the TM_{11} mode bears an electric field distribution with one antinode in the $\tilde{E}_z$-field (parallel to the NW) distribution inside the NW, indicating that it behaves as a resonant electric dipole. The linear electric dipole moment is given by $p_z = \alpha E_{z,inc}$, where α denotes the polarizability and $E_{z,inc}$ refers to the incident field at the center of the NW. We further assume that the polarizability α takes the simple form

$$\alpha = \frac{-i\kappa}{\tilde{\omega}_0 - \omega}, \qquad (1)$$

where $\tilde{\omega}_0 = \omega_0 - i\gamma_0$ is the complex frequency of the TM_{11} QNM and κ is a complex frequency-independent coefficient. We note that this single-pole formula is only approximative. It neglects the embodiment of higher-order multipoles, which are not fully negligible according to the QNM analysis. Its main strength is its simplicity and accuracy to quantitatively model the NW polarizability in the spectral range of interest. We retrieve $\tilde{\omega}_0$ from the QNM computation using the mode solver of COMSOL valid for nondispersive materials, and κ is obtained by fitting Eq. (1) with full-field simulation results α_{sim} of the polarizability obtained by integrating the local polarizability over the NW cross-section, $\alpha_{sim} = \int \varepsilon_0 (\varepsilon_{Si} - 1) E_z(\mathbf{r}) dS / E_{z,inc}(\mathbf{r} = 0)$. Here, $E_z(\mathbf{r})$ is the electric-field distribution of the NW under plane-wave illumination ($\mathbf{r} = 0$ is the center of the Si NW) and $\varepsilon_{Si} = 16$ is the relative
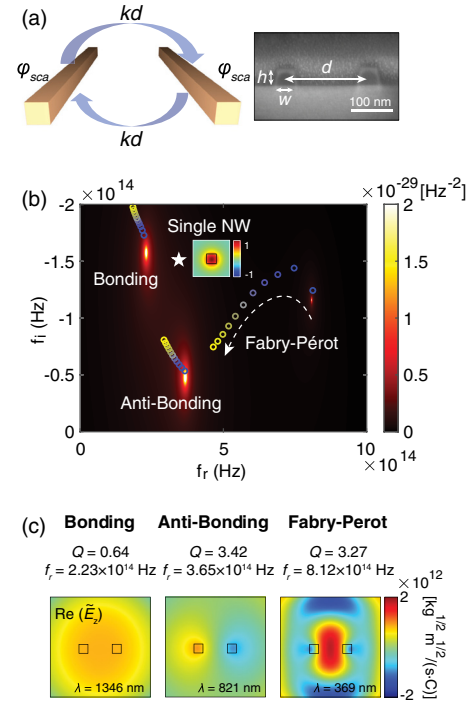
Fig. 1. Fabry–Pérot mode in a Si NW pair. (a) Left: QNM is formed as the result of light scattering back and forth between two neighboring NWs. Right inset: Cross-section scanning electron microscope (SEM) image of the fabricated Si NW pair. (b) Calculated reciprocal $1/\det(A(\tilde{\omega}))$ of the determinant of the 2×2 matrix used to model the coupled NW (dipole) system as a function of the real and imaginary parts of complex frequency $\tilde{\omega}$. The NW separation distance is 200 nm. The QNM frequencies computed with QNMEig for the bonding, antibonding, and Fabry–Pérot modes are overlaid as a function of the NW spacing from 200 nm (blue circles) to 400 nm (yellow circles) in steps of 20 nm. The $\tilde{E}_z$ field distribution of the dipolar TM_{11} QNM for a single NW (located at the white star position) is also plotted for reference. (c) Out-of-plane electric-field distributions $\tilde{E}_z(x, y)$ of the three simulated QNMs for a 200 nm spacing. In all plots, the modes are normalized with the PML-normalization method [52]. The normalization allows for a direct visual comparison of the interaction strength of the mode with driving field. All data are obtained for a 50 nm square size NW and for a Si permittivity $\varepsilon_{Si} = 16$.

permittivity of Si. The good agreement between α_{sim} and the fitted polarizability α (see Fig. S1 in Supplement 1), clearly indicates that Eq. (1) is a reasonable approximation.

Next, we focus on a Si NW pair system as shown in Fig. 1(a). We apply the coupled dipole theory [50,51] to simply take the interaction between NWs (effective linear dipoles p_1 and p_2) into account, so

$$\begin{pmatrix} i(\tilde{\omega}_0 - \tilde{\omega}) & -\kappa G(d, \tilde{\omega}) \\ -\kappa G(d, \tilde{\omega}) & i(\tilde{\omega}_0 - \tilde{\omega}) \end{pmatrix} \begin{pmatrix} p_1 \\ p_2 \end{pmatrix} = 0. \qquad (2)$$

The diagonal terms correspond to the intrinsic harmonic oscillation of the individual linear dipoles, where $\tilde{\omega}$ is the complex eigenfrequency of the system, and the off-diagonal terms represent the coupling between the two linear dipoles. $G(d, \tilde{\omega}) = \frac{ik^2}{4\varepsilon_0} H_0(kd)$ is the Green's function that defines the scattered field in terms of the dipole moment. H_0 is the zeroth-order Hankel function, d is the distance between the two effective

dipoles, and $k = \frac{\tilde{\omega}}{c}$ is the complex eigen wave vector for the coupled NWs. We emphasize that the off-diagonal term (i.e., the coupling strength) $g(\tilde{\omega}) = -\kappa G(d, \tilde{\omega})$ does not linearly depend on frequency. As a result, the determinant of the 2×2 matrix $\det(A(\omega)) = 0$ that is used to find the eigenvalues (or poles) of the coupled NW system is no longer simply the common quadratic polynomial in one variable $\tilde{\omega}$. The number of solutions is therefore no longer restricted to two [44].

The analysis above is in sharp contrast with most of the reported chemical bonding models [27–30] used to describe the coupling between two optical resonators, in which the off-diagonal term is usually assumed to be independent of frequency for a given system, and governed by the near-field overlap of the two resonators. We emphasize that such a fixed coupling-strength approximation is only valid if the coupling strength g is much smaller than the original complex frequency $\tilde{\omega}_0$. This is generally well-applicable for high-Q resonators for which the evanescent fields vanish very quickly away from the resonator surface. As a result, the mode splitting is relatively weak ($\tilde{\omega} \sim \tilde{\omega}_0$) and thus $g(\tilde{\omega})$ can be reasonably approximated by $g(\tilde{\omega}_0)$. However, this approximation fails for highly leaky optical resonators such as the fundamental TM_{11} Mie modes for Si NWs, where $Q \sim 1$. The radiative fields of these low-Q leaky modes have a natural phase evolution and grow exponentially in amplitude with the distance away from the resonator in the QNM profile [45,52,53]. This originates from the exponential decay of the amplitude of the mode in time domain. Therefore, the coupling strength g oscillates with increasing NW distance and can be comparable to the original frequency ω_0, resulting in a nonnegligible difference between $g(\tilde{\omega})$ and $g(\tilde{\omega}_0)$.

To show this, we apply the coupled dipole theory above to a 50 nm sized square Si (refractive index $n = 4$) NW pair with 200 nm center-to-center distance. The retrieved effective linear dipole polarizability for a single NW is $\frac{-i\kappa}{\tilde{\omega}_0 - \omega} = \frac{(6.1 - 5.2i) \times 10^{-11}}{(3.4 - 1.5i) \times 10^{14} - f}$ [F · m]. The reciprocal of the determinant of the 2×2 matrix $\mathrm{abs}(\frac{1}{-(\tilde{\omega}_0 - \tilde{\omega})^2 - \kappa^2 G^2(d, \tilde{\omega})})$ is plotted in the complex frequency plane, as shown in Fig. 1(b), such that the QNM frequencies occur as pole maxima. Three poles can be found within the frequency range of interest, indicating that there are at least three QNMs for the studied NW pair system. To verify the existence of the QNMs predicted with the dipole approximation, we perform full wave simulations with the COMSOL mode solver. We overlay the complex frequencies found from QNM simulations for a NW distance, ranging from 200 nm (blue circles) to 400 nm (yellow circles) in steps of 20 nm, to track the modal dispersion. The complex frequency of the TM_{11} QNM for a single NW (white star) is also shown for reference. We attribute the small difference between the frequencies obtained from the analytical poles and blue circles to the imprecise nature of Eq. (1). Figure 1(c) shows the out-of-plane electric field distribution of the three eigenmodes as retrieved with the numerical solver. We find that the first two of the three modes can be recognized as the conventional bonding (lower frequency) and antibonding (higher frequency) modes, mimicking the chemical bonding model. It should be noted that both show a red shift with increasing NW spacings and do not converge to the complex frequency of the original TM_{11} QNM for large d. This highlights the oscillating and frequency-dependent nature of the dipole–dipole coupling strength.

The third QNM, on the other hand, which exhibits an antinode in the air gap between the two NWs, is rather unique and is not predicted from the conventional chemical bonding model.
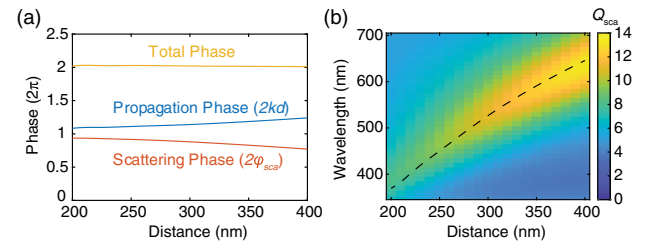
Fig. 2. Fabry–Pérot resonant nature of the new mode found for the Si NW pair. (a) Total phase (yellow), scattering phase (orange), and propagation phase (blue) of the Fabry–Pérot mode as a function of distance between two NWs. The phases are calculated at resonance using complex frequencies from numerical QNM simulation. (b) Simulated scattering efficiency of the Si NW pair as a function of incident wavelength and NW separation distance under normally incident, TM-polarized illumination. The black dashed line represents the center wavelengths of the Fabry–Pérot modes to increase NW separations as obtained from QNM simulations. The scattering efficiency is defined as the scattering cross-section normalized to the geometrical cross-section of two NWs.

The complex frequency of this mode shifts significantly from that of the original TM_{11} mode (single NW), revealing a considerable coupling strength between the neighboring NWs. We attribute the formation of this mode to a Fabry–Pérot resonance between two NWs, where light is iteratively scattered back and forth between the NWs. At resonance, two NWs are in phase as 2π is accumulated when light scattered from one NW to the other. To visualize this physical picture, we decompose the phase evolution into two parts: the scattering phase from of the NWs $\varphi_{sca} = \arg(\frac{-i\kappa}{\tilde{\omega}_0 - \tilde{\omega}_{FP}} \tilde{\omega}_{FP}^{3/2} e^{i\frac{\pi}{4}})$ and the propagation phase in the air gap $\varphi_{prop} = \mathrm{Re}(\frac{\tilde{\omega}_{FP}}{c} d)$. Figure 2(a) shows the phase decomposition results as a function of the NW separation distance d. We find that a constant 4π phase evolution is observed when the light travels back and forth in one round trip, regardless of d. This evidences the Fabry–Pérot nature of the QNM [43]. Note that higher-order Fabry–Pérot modes can also be found in the studied coupled NW system, as long as the $2n\pi$ ($n = 2, 3, \ldots$) phase is accumulated when light bounces back and forth in one round trip (see Supplement 1, Fig. S2).

The Fabry–Pérot QNM shows a stronger dispersion with the separation distance (200 nm $< d <$ 400 nm) compared to the bonding and antibonding modes, as shown in Fig. 1(b). The resonant frequency spans almost the entire visible frequency range from $\sim 4.6 \times 10^{14}$ Hz to 8.1×10^{14} Hz (corresponding to 370–650 nm) when the distance between the two NWs varies from 200 nm to 400 nm. As a result, we envision that the demonstrated Fabry–Pérot mode may function as a new type of universal building block to achieve structural color. Each unit cell would be composed of similar-sized nanostructures like photonic crystals, but with a varying NW spacing. Such a design also offers subwavelength resolution similar to resonant particles. Figure 2(b) shows the simulated scattering efficiency of the Si NW pair as a function of the incident wavelength and NW spacing under normally incident, TM-polarized illumination. A single scattering peak is observed for every NW spacing. The positions of the peaks perfectly overlap with the real parts of the complex frequencies predicted with the QNM simulations (black dashed curve). This additionally corroborates that the main scattering characteristic of NW pairs originates from the excitation of a Fabry–Pérot mode. In Supplement 1, Fig S3, we use the QNM expansion theory [53]

to quantitatively verify that the dominant contribution to the scattering cross-section spectrum of the pair is the Fabry–Pérot QNM.

The dispersion of Si has been neglected in the previous analysis, although both the real and imaginary parts of the refractive index of Si appreciably vary in the spectral region of the Fabry–Pérot QNM, for $\lambda < 450$ nm. To confirm the existence of that mode, we have repeated the QNM computations with a Si permittivity function consisting of pairs of Lorentz poles [54] and using either the QNM solvers QNMEig [53] or the freeware Modal Analysis of Nanoresonators (MAN) [55]. We find that the resonant frequency $\mathrm{Re}(\tilde{\omega}_{FP})$ of the Fabry–Pérot mode is only slightly changed by adding dispersion. This can be attributed to the fact that Fabry–Pérot and nanowire resonances, $\mathrm{Re}(\tilde{\omega}_{FP})$ and $\mathrm{Re}(\tilde{\omega}_0)$, are significantly different so that the propagation phase φ_{prop} dominantly sets the Fabry–Pérot condition. On the other hand, the quality factor is significantly decreased owing to the large value of $\mathrm{Im}(\varepsilon_{Si})$ at short wavelengths.

Additionally, with the solver QNMEig, we found that there exists a great number of higher-order modes with frequencies close to $\mathrm{Re}(\tilde{\omega}_{FP})$ for small NW spacings ($d < 250$ nm), for which the fields inside the Si NWs exhibit more than one anti-node. These higher-order modes also exist when the dispersion is turned off, but at frequencies much larger than $\mathrm{Re}(\tilde{\omega}_{FP})$. Dispersion pushes them closer to $\mathrm{Re}(\tilde{\omega}_{FP})$ because of the increased refractive index of Si at shorter wavelengths. We also note that some of these higher-order modes are characterized by strong fields in the air region between the two wires. In analogy to the Fabry–Pérot mode mentioned above which is caused by the nonlinear coupling between the dipolar modes of the wire, these modes are formed by the radiating coupling between wire multipole modes, and may thus be named multipolar Fabry–Pérot modes. When the resonator is excited by a monochromatic plane wave, both the higher-order modes (whether they are multipolar Fabry–Pérot modes or not) and the Fabry–Pérot mode can be excited, leading to a complicated response spectrum. In the experimental study discussed below, we mostly focus on NW pairs with Fabry–Pérot mode resonance

wavelengths larger than 450 nm, thus ignoring the dispersion Si makes for a reasonable assumption. Furthermore, the higher-order modes do not play an important role in the scattering response.

To experimentally demonstrate the color generation of the Si NW pair, we fabricate a series of Si NW pairs with varying NW spacing on a sapphire substrate using electron-beam lithography. The fabricated NWs all have a similar square cross-section, as shown in Fig. 1(a), with dimensions around 50 nm. The length of the NWs is chosen to be 50 µm to avoid finite-length effects [56]. Figure 3(a) shows the bright-field cross-polarized reflection optical image, in which Si NW pairs scatter different colors of light. The observed colors span almost all the way from the blue to red as a function of the NW spacing, confirming the potential of Si NW pairs as building blocks for structural color. The corresponding top-view scanning electron microscope images are shown in Fig. 3(b). We perform full-field simulations for the fabricated structures by taking the material dispersion and asymmetric dielectric environment into account. The simulated scattering efficiency spectra under normally incident, TM-polarized illumination are shown in Fig. 3(c). All the NW pairs show a strong, single scattering peak at a resonance wavelength between 490 and 650 nm as the distance between the NWs increases from 200 nm to 400 nm. Figure 3(d) shows the measured cross-polarized reflection spectra for different Si NW pairs that were taken using a confocal optical microscope. To filter out the direct reflection from the sapphire substrate, the incident beam is first polarized 45 deg with respect to the NW direction. Next, the scattered light is collected through a second polarizer that is oriented orthogonal to the first one. In this cross-polarized measurement scheme, only light scattered by the NWs is collected. In general, the measured reflection spectra are in good agreement with the simulated scattering efficiency spectra. The additional reflection peak around 500 nm may result from the nonuniform transmittance of the second polarizer, and small kinks in the spectra (560 nm, 610 nm, etc.) are caused by the interference in polarizer thin films. A higher scattering peak contrast is observed in the measurements as compared to the simulations in which the scatterings to all the angles are included. This is attributed to the
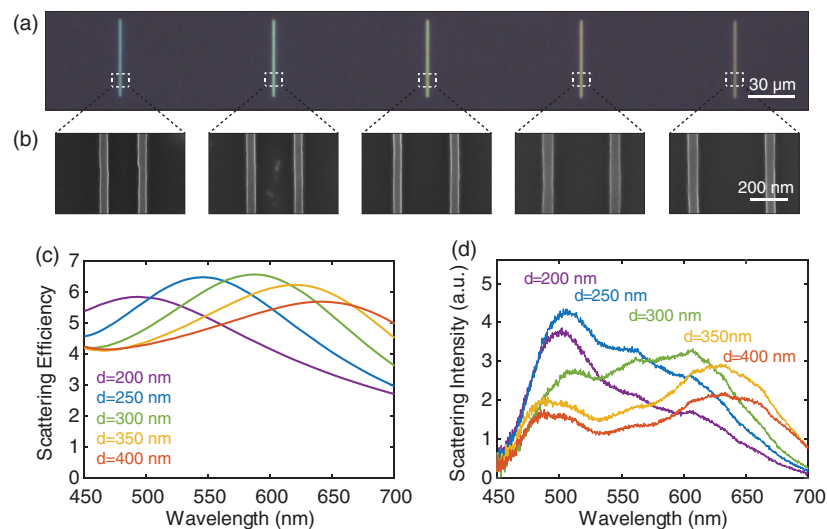
Fig. 3. Experimental demonstration of structural color from Si NW pairs. (a) Cross-polarized reflection optical image of the fabricated Si NW pairs. All the NWs are 50 µm long and have the same 50 nm square size. (b) Top-view scanning electron microscope images of fabricated Si NW pairs. The separation distance between the NWs increases from 200 nm to 400 nm in steps of 50 nm. (c) Simulated scattering efficiency of the designed Si NW pairs on the sapphire substrate as a function of the incident wavelength under normally incident, TM-polarized illumination. The dispersion and absorption of Si are considered in the simulation. (d) Measured cross-polarized reflection spectra for the different fabricated Si NW pairs.
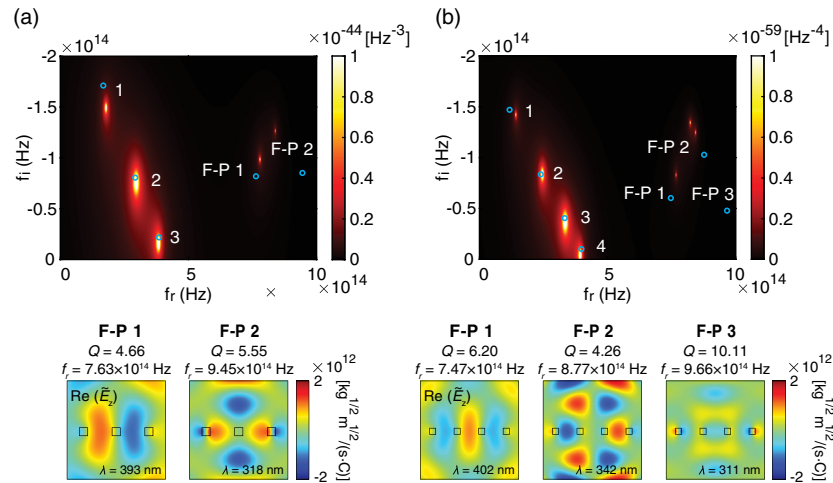
Fig. 4. Fabry–Pérot modes in Si NW arrays. Calculated reciprocal of the determinant of (a) the 3 × 3 matrix and (b) the 4 × 4 matrix used to describe the resonance modes of linear arrays composed of three or four NWs in a free space, as a function of the real and imaginary part of their complex frequencies. The NW separation distance is 200 nm. The complex frequencies of the QNMs computed with COMSOL for a constant Si permittivity are overlaid as blue circles. The out-of-plane electric field distributions of the corresponding Fabry–Pérot modes are shown in the lower panel.

fact that the scatterings from the excited Fabry–Pérot modes are highly directional normal to the substrate, which lies within the NA = 0.4 of the collection objective used in the measurement. We should note that the demonstrated structural color from the Si NW pairs has a strong polarization and angular dependence, which can be useful in novel applications such as transflective displays and optical information encryption.

Finally, we note that the Fabry–Pérot modes demonstrated above are not only supported by a NW pair, but can also be seen in assemblies comprised of a plurality of NWs. The Fabry–Pérot modes exist universally through the coupling between NWs (linear electric dipoles). The coupled dipole theory for n NWs can be generalized as

$$\sum_m A_{l,m} p_m = 0 \quad (l, m = 1, 2, \cdots, n),\qquad(3)$$

where $A_{l,l} = i(\tilde{\omega}_l - \tilde{\omega})$ and $A_{l,m\,(l\neq m)} = -\kappa_l G(d_{l,m}, \tilde{\omega})$. $\tilde{\omega}_l$ and κ_l are the complex eigenfrequency and coupling coefficient for the lth NW, and $d_{l,m}$ is the distance between the lth and mth NW. Figure 4 shows the reciprocal of the determinant of the 3 × 3 matrix and 4 × 4 matrix used to describe the coupling between three or four identical NWs arranged in parallel in free space, as a function of real and imaginary part of the complex frequency. Besides the conventional modes expected from the chemical bonding model (labeled as 1, 2, 3...), multiple Fabry–Pérot modes can also be found in both cases. The number of Fabry–Pérot modes of the same order supported is equal to the number of air gaps in the NW chain. The complex frequencies from numerical QNM simulations are overlaid with blue circles and are in good agreement with the analytical results (poles on the complex plane) under the dipole approximation. The electric field distributions of the simulated QNMs shown in Fig. 4 confirm the Fabry–Pérot resonant nature of these modes: The electric field is concentrated in the space between the neighboring wires. These Fabry–Pérot modes resonate at different wavelengths and can be labeled by their quasi in-plane momentum. Therefore, with a change of the incident angle, different Fabry–Pérot modes dominate the excitation, leading to the change of the scattering color. As the number of NWs

increases, we move from a regime in which a few discrete QNMs dominate the structural color response to a regime in which the well-known iridescence of periodic structures should take place with a continuum of QNMs indexed by the in-plane momentum wavenumber. The QNM at Γ point for a periodic structure [57] is a 1D cavity mode with symmetric radiation profiles with respect to the plane of NW array, and therefore renders the Si NW array at resonance as a perfect semiconductor metamirror [58], as shown in Supplement 1, Fig. S4.

In summary, we demonstrate both theoretically and experimentally that two identical neighboring Si NWs with different spacings form a new universal building block for structural color, while maintaining a subwavelength footprint. The structural color results from a series of Fabry–Pérot modes formed by light that is bouncing back and forth between two NW nanoresonators, and can be tuned across the entire visible spectrum by varying the interwire distance. These Fabry–Pérot modes are not expected from the conventional chemical bonding model. Instead, they can be well described by considering a nonlinear, frequency-dependent coupling between two NWs. The studied system presents what we believe, to the best of our knowledge, is a novel way to generate optical resonances in coupled nanostructures and expands the understanding of resonant coupling and the manipulation of light at the nanoscale.

REFERENCES AND NOTES

1. W. J. Joo, J. Kyoung, M. Esfandyarpour, S. H. Lee, H. Koo, S. Song, J. C. Bae, J. Ara, M. Kwon, S. H. Han, S. Hwang, and M. L. Brongersma, "Metasurface-driven OLED displays beyond 10,000 pixels per inch," Science **370**, 459–463 (2020).

2. C. Kittel, *Introduction to Solid State Physics* (Wiley, 1976).
3. Y. Zhao, Z. Xie, H. Gu, C. Zhu, and Z. Gu, "Bio-inspired variable structural color materials," Chem. Soc. Rev. **41**, 3297–3317 (2012).
4. S. D. Rezaei, Z. Dong, J. Y. E. Chan, J. Trisno, R. J. H. Ng, Q. Ruan, C. W. Qiu, N. A. Mortensen, and J. K. W. Yang, "Nanophotonic structural colors," ACS Photon. **8**, 18–33 (2021).
5. E. Yablonovitch, "Inhibited spontaneous emission in solid-state physics and electronics," Phys. Rev. Lett. **58**, 2059–2062 (1987).
6. S. John, "Strong localization of photons in certain disordered dielectric superlattices," Phys. Rev. Lett. **58**, 2486–2489 (1987).
7. J. D. Joannopoulos, P. R. Villeneuve, and S. Fan, "Photonic crystals: putting a new twist on light," Nature **386**, 143–149 (1997).
8. P. Vukusic, J. R. Sambles, and C. R. Lawrence, "Colour mixing in wing scales of a butterfly," Nature **404**, 457 (2000).
9. J. Huang, X. Wang, and Z. L. Wang, "Controlled replication of butterfly wings for achieving tunable photonic properties," Nano Lett. **6**, 2325–2331 (2006).
10. Y. A. Vlasov, X. Z. Bo, J. C. Sturm, and D. J. Norris, "On-chip natural assembly of silicon photonic bandgap crystals," Nature **414**, 289–293 (2001).
11. Y. Liu, H. Wang, J. Ho, R. C. Ng, R. J. Ng, V. H. Hall-Chen, E. H. H. Koay, Z. Dong, H. Liu, C. W. Qiu, J. R. Greer, and J. K. W. Yang, "Structural color three-dimensional printing by shrinking photonic crystals," Nat. Commun. **10**, 4340 (2019).
12. J. J. Mock, M. Barbic, D. R. Smith, D. A. Schultz, and S. Schultz, "Shape effects in plasmon resonance of individual colloidal silver nanoparticles," J. Chem. Phys. **116**, 6755–6759 (2002).
13. K. Kumar, H. Duan, R. S. Hegde, S. C. Koh, J. N. Wei, and J. K. W. Yang, "Printing colour at the optical diffraction limit," Nat. Nanotechnol. **7**, 557–561 (2012).
14. A. S. Roberts, A. Pors, O. Albrektsen, and S. I. Bozhevolnyi, "Subwavelength plasmonic color printing protected for ambient use," Nano Lett. **14**, 783–787 (2014).
15. S. Yokogawa, S. P. Burgos, and H. A. Atwater, "Plasmonic color filters for CMOS image sensor applications," Nano Lett. **12**, 4349–4354 (2012).
16. Y. Gu, L. Zhang, J. K. Yang, S. P. Yeo, and C. W. Qiu, "Color generation via subwavelength plasmonic nanostructures," Nanoscale **7**, 6409–6419 (2015).
17. S. D. Rezaei, R. J. H. Ng, Z. Dong, J. Ho, E. H. Koay, S. Ramakrishna, and J. K. Yang, "Wide-gamut plasmonic color palettes with constant subwavelength resolution," ACS Nano **13**, 3580–3588 (2019).
18. A. Kristensen, J. K. Yang, S. I. Bozhevolnyi, S. Link, P. Nordlander, N. J. Halas, and N. A. Mortensen, "Plasmonic colour generation," Nat. Rev. Mater. **2**, 16088 (2016).
19. M. Song, D. Wang, S. Peana, S. Choudhury, P. Nyga, Z. A. Kudyshev, H. Yu, A. Boltasseva, V. M. Shalaev, and A. V. Kildishev, "Colors with plasmonic nanostructures: a full-spectrum review," Appl. Phys. Rev. **6**, 041308 (2019).
20. L. Cao, P. Fan, E. S. Barnard, A. M. Brown, and M. L. Brongersma, "Tuning the color of silicon nanostructures," Nano Lett. **10**, 2649–2654 (2010).
21. A. I. Kuznetsov, A. E. Miroshnichenko, Y. H. Fu, J. Zhang, and B. Luk'yanchuk, "Magnetic light," Sci. Rep. **2**, 492 (2012).
22. V. Flauraud, M. Reyes, R. Paniagua-Dominguez, A. I. Kuznetsov, and J. Brugger, "Silicon nanostructures for bright field full color prints," ACS Photon. **4**, 1913–1919 (2017).
23. P. Huo, M. Song, W. Zhu, C. Zhang, L. Chen, H. J. Lezec, Y. Lu, A. Agrawal, and T. Xu, "Photorealistic full-color nanopainting enabled by a low-loss metasurface," Optica **7**, 1171–1172 (2020).
24. W. Yang, S. Xiao, Q. Song, Y. Liu, Y. Wu, S. Wang, J. Yu, J. Han, and D. P. Tsai, "All-dielectric metasurface for high-performance structural color," Nat. Commun. **11**, 1864 (2020).
25. M. A. Verschuuren, M. W. Knight, M. Megens, and A. Polman, "Nanoscale spatial limitations of large-area substrate conformal imprint lithography," Nanotechnology **30**, 345301 (2019).
26. H. Lan, *Soft UV Nanoimprint Lithography and its Applications* (InTech, 2013).
27. P. Nordlander, C. Oubre, E. Prodan, K. Li, and M. I. Stockman, "Plasmon hybridization in nanoparticle dimers," Nano Lett. **4**, 899–903 (2004).
28. E. Prodan, C. Radloff, N. J. Halas, and P. Nordlander, "A hybridization model for the plasmon response of complex nanostructures," Science **302**, 419–422 (2003).
29. P. K. Jain, S. Eustis, and M. A. El-Sayed, "Plasmon coupling in nanorod assemblies: optical absorption, discrete dipole approximation simulation, and exciton-coupling model," J. Phys. Chem. B **110**, 18243–18253 (2006).
30. S. Sheikholeslami, Y. W. Jun, P. K. Jain, and A. P. Alivisatos, "Coupling of optical resonances in a compositionally asymmetric plasmonic nanoparticle dimer," Nano Lett. **10**, 2655–2660 (2010).
31. J. S. Clausen, E. Højlund-Nielsen, A. B. Christiansen, S. Yazdi, M. Grajower, H. Taha, U. Levy, A. Kristensen, and N. A. Mortensen, "Plasmonic metasurfaces for coloration of plastic consumer products," Nano Lett. **14**, 4499–4504 (2014).
32. H. Lochbihler and Y. Ye, "Two-dimensional subwavelength gratings with different frontside/backside reflectance," Opt. Lett. **38**, 1028–1030 (2013).
33. L. Cao, P. Fan, and M. L. Brongersma, "Optical coupling of deep-subwavelength semiconductor nanowires," Nano Lett. **11**, 1463–1468 (2011).
34. L. Gunnarsson, T. Rindzevicius, J. Prikulis, B. Kasemo, M. Käll, S. Zou, and G. C. Schatz, "Confined plasmons in nanofabricated single silver particle pairs: experimental observations of strong interparticle interactions," J. Phys. Chem. B **109**, 1079–1087 (2005).
35. J. van de Groep, T. Coenen, S. A. Mann, and A. Polman, "Direct imaging of hybridized eigenmodes in coupled silicon nanoparticles," Optica **3**, 93–99 (2016).
36. J. Aizpurua, G. W. Bryant, L. J. Richter, F. G. De Abajo, B. K. Kelley, and T. Mallouk, "Optical properties of coupled metallic nanorods for field-enhanced spectroscopy," Phys. Rev. B **71**, 235420 (2005).
37. I. Romero, J. Aizpurua, G. W. Bryant, and F. J. G. De Abajo, "Plasmons in nearly touching metallic nanoparticles: singular response in the limit of touching dimers," Opt. Express **14**, 9988–9999 (2006).
38. B. Lamprecht, G. Schider, R. T. Lechner, H. Ditlbacher, J. R. Krenn, A. Leitner, and F. R. Aussenegg, "Metal nanoparticle gratings: influence of dipolar particle interaction on the plasmon resonance," Phys. Rev. Lett. **84**, 4721 (2000).
39. B. Auguié and W. L. Barnes, "Collective resonances in gold nanoparticle arrays," Phys. Rev. Lett. **101**, 143902 (2008).
40. C. Dahmen, B. Schmidt, and G. von Plessen, "Radiation damping in metal nanoparticle pairs," Nano Lett. **7**, 318–322 (2007).
41. C. L. Haynes, A. D. McFarland, L. Zhao, R. P. Van Duyne, G. C. Schatz, L. Gunnarsson, J. Prikulis, B. Kasemo, and M. Käll, "Nanoparticle optics: the importance of radiative dipole coupling in two-dimensional nanoparticle arrays," J. Phys. Chem. B **107**, 7337–7342 (2003).
42. S. Yi, M. Zhou, Z. Yu, P. Fan, N. Behdad, D. Lin, K. X. Wang, S. Fan, and M. L. Brongersma, "Subwavelength angle-sensing photodetectors inspired by directional hearing in small animals," Nat. Nanotechnol. **13**, 1143–1147 (2018).
43. R. Taubert, R. Ameling, T. Weiss, A. Christ, and H. Giessen, "From near-field to far-field coupling in the third dimension: retarded interaction of particle plasmons," Nano Lett. **11**, 4421–4424 (2011).
44. A. A. Dmitriev and M. V. Rybin, "Combining isolated scatterers into a dimer by strong optical coupling," Phys. Rev. A **99**, 063837 (2019).
45. P. Lalanne, W. Yan, K. Vynck, C. Sauvan, and J. P. Hugonin, "Light interaction with photonic and plasmonic resonances," Laser Photon. Rev. **12**, 1700113 (2018).
46. E. Arbabi, A. Arbabi, S. M. Kamali, Y. Horie, M. Faraji-Dana, and A. Faraon, "MEMS-tunable dielectric metasurface lens," Nat. Commun. **9**, 812 (2018).
47. A. L. Holsteen, S. Raza, P. Fan, P. G. Kik, and M. L. Brongersma, "Purcell effect for active tuning of light scattering from semiconductor optical antennas," Science **358**, 1407–1410 (2017).
48. G. Mie, "Beiträge zur optik trüber medien, speziell kolloidaler metallösungen," Ann. Phys. **330**, 377–445 (1908).
49. L. Cao, J. S. White, J. S. Park, J. A. Schuller, B. M. Clemens, and M. L. Brongersma, "Engineering light absorption in semiconductor nanowire devices," Nat. Mater. **8**, 643–647 (2009).
50. A. Yariv, "Coupled-mode theory for guided-wave optics," IEEE J. Quantum Electron. **9**, 919–933 (1973).
51. H. A. Haus and W. Huang, "Coupled-mode theory," Proc. IEEE **79**, 1505–1518 (1990).
52. C. Sauvan, J. P. Hugonin, I. S. Maksymov, and P. Lalanne, "Theory of the spontaneous optical emission of nanosize photonic and plasmon resonators," Phys. Rev. Lett. **110**, 237401 (2013).
53. W. Yan, R. Faggiani, and P. Lalanne, "Rigorous modal analysis of plasmonic nanoresonators," Phys. Rev. B **97**, 205422 (2018).

54. M. Garcia-Vergara, G. Demésy, and F. Zolla, "Extracting an accurate model for permittivity from experimental data: hunting complex poles from the real line," Opt. Lett. **42**, 1145–1148 (2017).

55. The QNM solvers and COMSOL models of the software MAN (Modal Analysis of Nanoresonators) can be downloaded at https://www.lp2n.institutoptique.fr/light-complex-nanostructures.

56. H. S. Ee, J. H. Kang, M. L. Brongersma, and M. K. Seo, "Shape-dependent light scattering properties of subwavelength silicon nanoblocks," Nano Lett. **15**, 1759–1765 (2015).

57. Q. Li, J. van de Groep, Y. Wang, P. G. Kik, and M. L. Brongersma, "Transparent multispectral photodetectors mimicking the human visual system," Nat. Commun. **10**, 4982 (2019).

58. P. Ghenuche, G. Vincent, M. Laroche, N. Bardou, R. Haïdar, J. L. Pelouard, and S. Collin, "Optical extinction in a single layer of nanorods," Phys. Rev. Lett. **109**, 143903 (2012).